October 27th, 2023

Faraday Waves in Gas-Fluidized Beds Subject to Combined Vertical and Horizontal Vibration

Javad Omidi¹, Oscar J. Punch¹, Qiang Guo¹, Christopher M. Boyce^{1*}

¹Department of Chemical Engineering, Columbia University, New York, NY 10027, USA *Corresponding Author. Email: cmb2302@columbia.edu

Abstract

The dynamics of Faraday waves in a gas-fluidized bed vibrated in both the vertical and horizontal directions simultaneously were investigated using two-fluid model (TFM) simulations. Prior experimental and numerical studies have demonstrated the formation of Faraday waves in gas-fluidized beds, and the TFM simulations here are validated against prior experimental studies. The novelty of this study is subjecting a gas-fluidized bed to combined vertical and horizontal vibrations. The key physical insights are that (1) Faraday waves can still form when horizontal vibration is added and (2) the horizontal mixing rate and extent increases markedly by adding horizontal vibration. Further, non-dimensional empirical correlations and regime maps for wavelength and wave height were established based on dimensional analysis. Increasing vertical vibration frequency decreased horizontal mixing, yet increasing horizontal vibration frequency increased horizontal mixing. Increasing gas flow rate increased the rate of vertical mixing, but decreased the rate of horizontal mixing.

Keywords: Fluidization, granular materials, mixing, segregation, Faraday waves

1. Introduction

Fluidization is a process in which granular particles are suspended in a fluid-like state, typically either via upward gas flow or vertical vibration overcoming gravitational force on the particles [1,2]. Fluidized beds are containers of fluidized particles and often used to induce particle mixing, heat transport and contact between gas and particles. Structures analogous to those in conventional fluids, notably gas bubbles [1,3] and Faraday waves [4,5], have been reported in fluidized beds subjected to either gas flow or vibration. These bubbles and surface waves can act to create bulk convection which mixes the particles, which is desirable for a range of industrial applications [6,7].

Prior studies on Faraday waves were first conducted in granular beds subject to vertical vibration alone and shown to form with and without the presence of interstitial gas [4,6,8,9]. Wave patterns tend to repeat themselves every two vibration periods due to collisions between particles and the bottom plate every vibration period causing a reversal of horizontal momentum in the particles which results in a reversal in crests and troughs in the waves [10]. Experiments showed the wavelength (λ) scaling linearly with f_v^{-2} in which f_v is the frequency of vertical vibrations, leading to the development of dispersion relationships to correlate for wavelength [11]. Experiments were conducted in both pseudo-2D systems, which are narrow in one horizontal direction to only allow for 2D waves [4], as well as 3D systems which allow for the formation of 3D wave patterns [6]. Non-dimensionalization of the phenomenon has identified the vertical vibration strength:

$$\Gamma_v^* = 4\pi^2 f_v^2 A_v g^{-1} \tag{1}$$

and normalized frequency:

$$f_v^* = f_v H^{1/2} g^{-1/2} \tag{2}$$

to be key parameters for describing the wave patterns and wavelength formed [6,11]. In Equations (1) and (2), A_v is the amplitude of vertical vibration, g is gravitational acceleration and H is the height of particles in the bed. Further studies have shown that Faraday waves can also form in gas-fluidized beds with no vibration subject to oscillating upward gas flow, with similar patterns observed [5]. While most industrial applications use bubbling to induce mixing in particles, bubble dynamics are typically chaotic and change with system size, making fluidized bed processes difficult to scale-up and optimize [12,13]. As such, the predictable, ordered dynamics of Faraday waves offer potential for use in industrial processes, addressing issues with scale-up of bubbling fluidized beds [12,14,15].

Vertically vibrated gas-fluidized beds have been used industrially largely to fluidize particles which would be difficult to fluidize with gas flow alone due to cohesive forces between particles [16]. Recently, vibrated gas-fluidized beds have been demonstrated to induce structured flow patterns in gas fluidized beds [17], including bubble-free convection cells [18], Rayleigh-Taylor instabilities [19], structured bubbling [14] and Faraday waves [15]. The combined vibration and gas flow showed that Faraday waves could form at lower vibration strengths and persist to taller bed heights than using vibration alone, expanding the industrial potential for use [15].

However, the compartmentalized convective behavior of structured flow phenomena, such as Faraday waves and structured bubbling, potentially limits the rate of horizontal mixing [7].

While most studies of vibrating granular material and Faraday waves have involved vertical vibration, a number of prior studies have involved horizontal vibration. For fluidized beds, Ristow et al. [20] investigated the transition from solid-like to fluid-like behavior of granular material in a horizontally vibrated fluidized bed, observing unique convection patterns in horizontally vibrating granular material. Another study noted conditions for the onset of flow in horizontally vibrated 3D granular systems [21]. Medved et al. investigated the response of granular material to horizontal vibrations across various time scales [22]. Another study analyzed the movement of a single bubble in a fluidized bed, examining the influence of horizontal and vertical vibration directions on bubble behavior [23]. For surface waves, Khan and Eslamian [24] conducted experiments to investigate the synchronous nature of primary surface waves that form on a thin layer of water pinned to a glass surface and exposed to horizontal vibrations. Their findings revealed that the stability or instability of the surface waves depended on the amplitude and frequency of the vibrations and the thickness of the liquid layer.

Gas-granular flows have been simulated in a number of ways [25–28], typically using continuum computational fluid dynamics (CFD) to model the gas phase, but differing in ways to model particles as well as gas-particle interactions. At the smallest scale, each particle can be modeled individually using the discrete element method (DEM) and CFD with grid sizes small enough to capture the no-slip boundary condition on the particles can be used [28]; however, these methods are too computationally expensive for most laboratory-scale fluidized beds. To simulate smaller laboratory-scale fluidized beds, the CFD-DEM method [25] is used in which particles are resolved individually [29], and CFD with grid cells larger than the particles are used to capture gas flow [30] with the two coupled using a drag law [31]. To simulate larger laboratory-scale systems and move toward industrial systems, two-fluid modeling (TFM) is often used, in which both gas and solids are modeled as interpenetrating continua using CFD [27]. In TFM, the solids phase is modeled as a non-Newtonian fluid to account for dissipative and frictional particle contacts [32], and the two phases interact via a drag law [31].

Here, we study the effect of combined vertical and horizontal vibration on Faraday waves and particle mixing in vibrated gas-fluidized beds numerically using experimentally validated TFM simulations. We vary vertical and horizontal vibration conditions separately as well as gas flow conditions to create regime maps and non-dimensional correlations for wave dynamics as well as quantification of horizontal and vertical mixing over time.

2. Methods

2.1 TFM Model Equations

For conducting the TFM simulations, the open source MFiX software [33] from the National Energy Technology Laboratory was employed. TFM is an approach for studying multiphase systems, in which the gas and solids phases are considered as fully interpenetrating continua [27]. Both phases coexist and interact within the system, with separate, locally-averaged

Navier-Stokes equations [30] used to solve their respective motions on a same fluid grid. The gas phase is governed by the continuity and momentum equations, which describe the conservation of mass and momentum of the phase:

$$\frac{\partial(\varepsilon_g \rho_g)}{\partial t} + \nabla \cdot \left(\varepsilon_g \rho_g \vec{u}_g\right) = 0 \tag{3}$$

$$\frac{\partial(\varepsilon_g \rho_g \vec{u}_g)}{\partial t} + \nabla \cdot \left(\varepsilon_g \rho_g \vec{u}_g \vec{u}_g\right) = -\varepsilon_g \nabla p_g + \nabla \cdot \overline{\bar{\tau}}_g + \varepsilon_g \rho_g \vec{g} + \beta (\vec{u}_s - \vec{u}_g) \tag{4}$$

Here, ε_g , ρ_g , \vec{u}_g , p_g and $\bar{\tau}_g$ are the void fraction, density, velocity, pressure and stress of the gas phase, respectively. \vec{g} is the gravitational acceleration and t is the time. The stress tensor of the gas phase $\bar{\tau}_g$ is determined under the assumption of Newtonian behavior:

$$\overline{\bar{\tau}}_g = \mu_g \left(\nabla \vec{u}_g + \nabla \vec{u}_g^T \right) - \frac{2}{3} \mu_g (\nabla \cdot \vec{u}_g) \overline{\bar{I}}$$
 (5)

where μ_q and \bar{I} are the viscosity of the gas phase and identity tensor, respectively.

The solids phase is characterized by its own continuity and momentum equations, governing the conservation of mass and momentum within this phase:

$$\frac{\partial(\varepsilon_s \rho_s)}{\partial t} + \nabla \cdot (\varepsilon_s \rho_s \vec{u}_s) = 0 \tag{6}$$

$$\frac{\partial(\varepsilon_s \rho_s \vec{u}_s)}{\partial t} + \nabla \cdot (\varepsilon_s \rho_s \vec{u}_s \vec{u}_s) = -\varepsilon_s \nabla p_g - \nabla p_s + \nabla \cdot \overline{\bar{\tau}}_s + \varepsilon_s \rho_s \vec{g} + \beta (\vec{u}_g - \vec{u}_s)$$
 (7)

where ε_s , ρ_s , \vec{u}_s , p_s and $\bar{\tau}_s$ are the volume fraction, density, velocity, pressure and stress of the solids phase, respectively. The stress tensor of the solids phase, denoted as $\bar{\tau}_s$, is computed using the following equation:

$$\overline{\overline{\tau}}_{s} = \mu_{s} (\nabla \vec{u}_{s} + \nabla \vec{u}_{s}^{T}) - \frac{2}{3} \mu_{s} (\nabla \cdot \vec{u}_{s}) \overline{\overline{I}}$$
(8)

where μ_s is the non-Newtonian viscosity (described below) of the solids phase.

In Equations (4) and (7), the momentum exchange coefficient (β) between the gas phase and solids phase is obtained by solving the Gidaspow drag law [31]. This law provides a relationship that quantifies the drag forces experienced by the gas and solids phases during their interaction:

$$\beta = \begin{cases} 150 \frac{(1 - \varepsilon_g)\mu_g}{\varepsilon_g d_s^2} + 1.75 \frac{\rho_g |\vec{u}_g - \vec{u}_s|}{d_s} & \varepsilon_g < 0.8\\ \frac{3}{4} C_D \frac{\rho_g |\vec{u}_g - \vec{u}_s| \varepsilon_g^{-1.65}}{d_s} & \varepsilon_g \ge 0.8 \end{cases}$$

$$(9)$$

$$C_D = \begin{cases} 0.44 & Re > 1000\\ \frac{24}{Re} (1 + 0.15Re^{0.687}) & Re \le 1000 \end{cases}$$
 (10)

$$Re = \frac{\rho_g \varepsilon_g d_s |\vec{u}_g - \vec{u}_s|}{\mu_g} \tag{11}$$

where d_s , C_D , and Re are the particle diameter of the solids phase, drag coefficient and Reynolds number, respectively.

The solids pressure (p_s) and solids viscosity (μ_s) include both kinetic and frictional contributions, reflecting the combined effects of particle movement and interactions within the solids phase. These contributions are crucial in accurately characterizing the behavior and flow properties of the solids phase in multiphase systems:

$$p_s = p_s^k + p_s^f \tag{12}$$

$$\mu_S = \mu_S^k + \mu_S^f \tag{13}$$

where the superscripts k and f indicate the kinetic and frictional contributions, respectively. The kinetic theory of granular flows (KTGF) developed by Lun et al. [32] provides a comprehensive framework for determining the pressure and viscosity of solids resulting from kinetic effects. The complete set of equations defining these properties used in the numerical model here can be found in Musser and Carney [33]. The modeling of granular motion and void fraction largely relies on an appropriate model for determining the solids pressure and solids viscosity resulting from frictional effects. Among the available models, we used that developed by Guo et al. [14] because it has been demonstrated to accurately predict structured granular flow [14,15] without needing any modifications to the gas flow or vibration conditions encountered in experimental scenarios. The model proposed by Guo et al. [14] employs a critical state solids pressure formulation that is derived from a shear-induced dilation law [34,35] developed in Discrete Element Method (DEM) simulations. This formulation is built upon the Srivastava and Sundaresan model [36]. To address issues related to discontinuity, additional terms from the solids pressure formulation in the Schaeffer model [37] are incorporated. The complete expressions for the solids pressure and solids viscosity formulations in the Guo et al. [14] model can be found in Equations (14) – (16):

$$= \begin{cases}
\frac{\left[\left(\varepsilon_{s,max} - \varepsilon_{s,minf}\right)\sqrt{2\overline{\overline{S}}:\overline{\overline{S}}}d_{s}\right]^{2}\rho_{p}}{\delta^{2}} + A_{pc}\left(\varepsilon_{s} + \delta - \varepsilon_{s,max}\right)^{n_{pc}} & \varepsilon_{s} > (\varepsilon_{s,max} - \delta) \\
\frac{2 \times \arctan\left[10^{4} \times \left(\varepsilon_{s} - \varepsilon_{s,minf}\right)\right]}{\pi} \frac{\left[\left(\varepsilon_{s,max} - \varepsilon_{s,minf}\right)\sqrt{2\overline{\overline{S}}:\overline{\overline{S}}}d_{s}\right]^{2}\rho_{s}}{\left(\varepsilon_{s,max} - \varepsilon_{s}\right)^{2}} & \varepsilon_{s,minf} \leq \varepsilon_{s} \leq (\varepsilon_{s,max} - \delta) \\
0 & \varepsilon_{s} < \varepsilon_{s,minf}
\end{cases} \tag{14}$$

$$\frac{p_s^f}{p_c} = \left[1 - \frac{\nabla \cdot \vec{u}_s}{n\sqrt{2}\sin(\phi)\sqrt{\overline{S}}:\overline{S} + \Theta_s/d_s^2}\right]^{n-1}$$
(15)

$$\mu_s^f = \frac{\sqrt{2}p_s^f \sin(\phi)}{2\sqrt{\overline{S}}: \overline{S} + \theta_s/d_s^2} \left[n - (n-1)(\frac{p_s^f}{p_c})^{\frac{1}{n-1}} \right]$$
(16)

Here, p_c represents the solids pressure at a critical state, in which the granular assembly undergoes deformation without any change in volume. $\varepsilon_{s,max}$ refers to the packing limit, which represents the maximum achievable solids concentration. $\varepsilon_{s,minf}$ denotes the critical solids concentration above which the frictional contributions are taken into consideration. Θ_s represents the granular temperature, which characterizes the fluctuating kinetic energy in the grains. ϕ represents the angle of internal friction, which is a measure of the resistance to shear deformation in the granular material. δ is a small constant value. A_{pc} and n_{pc} are two constants in the Schaeffer model [37] that are adapted and included in the formulation to avoid issues related to discontinuity.

 $\overline{\overline{S}}$ in Equations (14) – (16) represents the deviatoric rate-of-strain tensor of the solids phase.:

$$\overline{\overline{S}} = \frac{1}{2} (\nabla \vec{u}_S + \nabla \vec{u}_S^T) - \frac{1}{3} (\nabla \cdot \vec{u}_S) \overline{\overline{I}}$$
(17)

The exponent n in Equations (15) and (16) takes distinct values depending on whether the granular assembly is undergoing dilation or compaction.

$$n = \begin{cases} \frac{\sqrt{3}}{2\sin(\phi)} & \nabla \cdot \vec{u}_s \ge 0\\ 1.03 & \nabla \cdot \vec{u}_s < 0 \end{cases}$$
(18)

To quantify the mixing in various bed cases, an additional passive scalar equation is utilized to track the mass fraction of a tracer in the solids phase:

$$\frac{\partial(\varepsilon_s \rho_s x_s)}{\partial t} + \nabla \cdot (\varepsilon_s \rho_s x_s \vec{u}_s) = 0 \tag{19}$$

where x_s is the mass fraction of the tracer in the solids phase.

2.2 Simulation Setup

As illustrated in Figure 1, the pseudo-2D fluidized bed simulation was conducted with dimensions: 100 mm in width, 80 mm in height and 2 mm in depth. A reduction in bed freeboard height and bed depth as compared to prior experimental studies [15] was implemented to effectively reduce the computational costs. The simulated gas phase was characterized by a density of 1.2 kg/m³ and a viscosity of 1.8×10^{-5} Pa·s. The simulated solid phase was characterized by a density of 2500 kg/m³ and a particle size of 250 µm. The packing limit $\varepsilon_{s,max}$, critical solid concentration above which frictional contributions to solid stress are considered $\varepsilon_{s,minf}$, restitution coefficient, and angle of internal friction ϕ were set at 0.63, 0.5, 0.95, and 28.5°, respectively.

A structured mesh was used with a uniform size of 1 mm in all directions, which corresponds to four particle diameters. The initial configuration involved loading the solids phase into the bed at a volume fraction of 0.55, with a solids fill height of H = 30 mm, as illustrated schematically in Figure 1. A constant superficial gas velocity, denoted as U, was applied as the

inlet boundary condition, uniform across the entire base of the fluidized bed. This velocity was determined to be 1.04 U_{mf} , which was obtained from a separate simulation. This gas inlet condition was used to match the gas inlet in prior experiments [15], which used a porous sintered metal plate as the distributor to ensure a uniform gas inlet velocity. In the separate simulation, the superficial gas velocity was gradually reduced linearly from a state of strong bubbling to that of a packed bed while the bed pressure drop was continuously monitored. U_{mf} was determined to be 0.048 m/s from this simulation. The outlet boundary condition maintained a constant atmospheric pressure. Side walls were considered periodic for both the gas and solids phases. Detailed parameters used in the simulations are provided in Table 1.

Rather than vibrating the entire setup as done in experimental studies using a shaker [15], vibration effects were incorporated by oscillating gravity according to the equations: $\overrightarrow{g_v} = 9.81 +$ $(2\pi f_v)^2 A_v \sin(2\pi f_v t)$ for vertical vibration, and $\overrightarrow{g_h} = (2\pi f_h)^2 A_h \sin(2\pi f_h t)$ for horizontal vibration. The rationale behind applying this modeling approach was to reduce the computational costs and the lack of a moving mesh feature in MFiX. From the perspective of the laboratory reference frame, this modeling approach deviates from the actual experimental setup, where the bottom particles engage in collisions with the moving bottom boundary and the side wall particles experience frictional contacts while the central bed particles are less impacted by the applied vibration. Modeling vibration via oscillating gravity affects all particles uniformly, unlike real experiments with distinct localized impacts. Thus, deviations from experiments may arise. However, from the perspective of the vibrating fluidized bed, oscillating gravity is the only change to the governing equations needed to describe the entire fluidized bed moving up-and-down and side-to-side, as demonstrated in full mathematical detail and validated previously [38]. As such, modeling the vibration via oscillating gravity can be viewed as capturing the full physics of vibration, just through a moving reference frame rather than the laboratory reference frame. For the sake of obtaining a regime map of the Faraday wave pattern, the vibration amplitude was kept constant at 2 mm for all cases. However, the horizontal frequency varied between 2 and 24 Hz, while the vertical frequency ranged from 5 to 24 Hz.

Table 1. TFM Simulation parameters

Quantity	Symbol	Unit	Value
System geometry	$L_x \times L_y \times L_z$	mm	$100 \times 80 \times 2$
Number of CFD cells	$N_x \times N_y \times N_z$	-	$100 \times 80 \times 2$
Gas density	$ ho_g$	kg/m^3	1.2
Gas viscosity	μ_g	Pa·s	1.8×10^{-5}
Solids density	$ ho_s$	kg/m^3	2500
Solids size	d_s	μm	250
Initial particle height	H_B	mm	30
Initial packing concentration	$arepsilon_{s,init}$	-	0.55
Restitution coefficient	e	-	0.95
Angle of internal friction	ϕ	0	28.5
Angle of wall friction	ϕ_w	0	12.3
Packing limit	$\varepsilon_{s,max}$	-	0.63
Critical solids concentration	$\mathcal{E}_{s,minf}$	-	0.5
Drag law model	-	-	Gidaspow [26]
Viscous solids stress model	-	-	Lun et al. [28]
Frictional solids stress model	-	-	Guo et al. [8]
Time step	dt	S	1×10^{-4}
Temporal discretization scheme	-	-	Implicit Euler
Spatial discretization scheme	-	-	Superbee
Horizontal Vibration frequency	f	Hz	2 - 24
Vertical Vibration frequency	f	Hz	5 - 24
Horizontal Vibration amplitude	$\stackrel{\cdot}{A}$	mm	2.0
Vertical Vibration amplitude	A	mm	2.0

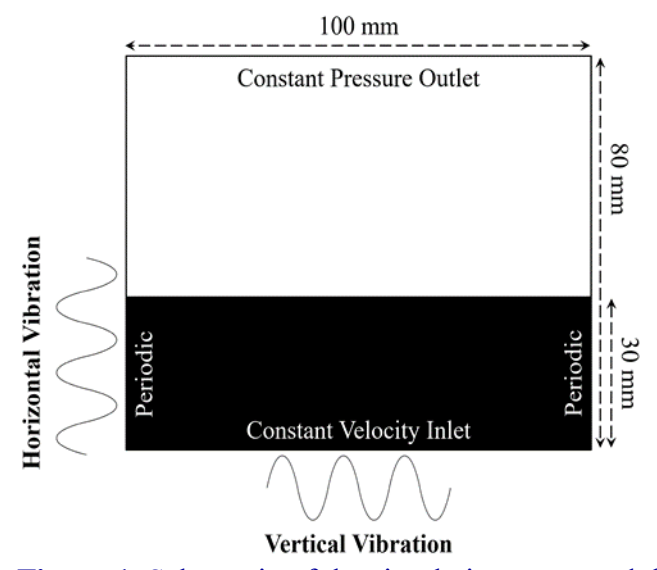


Figure 1. Schematic of the simulation setup and dimensions.

2.3 Data Processing

The wavelength and height (shown in Figure 2) were determined using digital image analysis based on the gas void fraction distribution. Initially, the gas void fraction distribution was averaged along the depth direction. Subsequently, a void fraction threshold of 0.75 was applied to binarize the distribution into two regions, allowing the identification of gas regions where the void

fraction exceeded 0.75. The average wavelength was computed as the distance between two consecutive wave crests, while the wave height was determined as the vertical distance between the wave's trough and its crest. Standard deviation values were also calculated for both wavelength and wave height to quantify their variations.

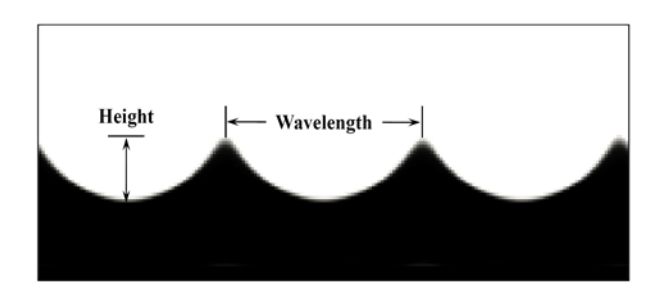


Figure 2. Schematic of the determination of the wavelength and wave height.

To investigate the mixing characteristics in various vertical bed configurations, the bed was initially divided into four regions of equal volume along its height. The tracer's mass fraction in the solid phase, x_s , was set to 0 in the first and third regions, while x_s was set to 1 in the remaining two regions, as depicted in Figure 3 (a). A similar approach was used to evaluate the vertical mixing, as illustrated in Figure 3 (b). The degree of mixing within the bed, based on the tracer's distribution in the solid phase, was quantified by analyzing the Segregation Intensity (SI) [39]:

$$SI = \frac{\sigma(x_S)}{\sqrt{\frac{N_{tracer}}{N_{total}}} (1 - \frac{N_{tracer}}{N_{total}})}$$
(20)

where $\sigma(x_S)$ represents the standard deviation of the tracer particles' mass fraction within all the CFD cells. N_{tracer} and N_{total} denote the total number of tracer particles and the total number of particles in the system [9]. The SI ranges from 0 to 1, where a value of 0 indicates a fully mixed state, and a value of 1 corresponds to a fully segregated state.

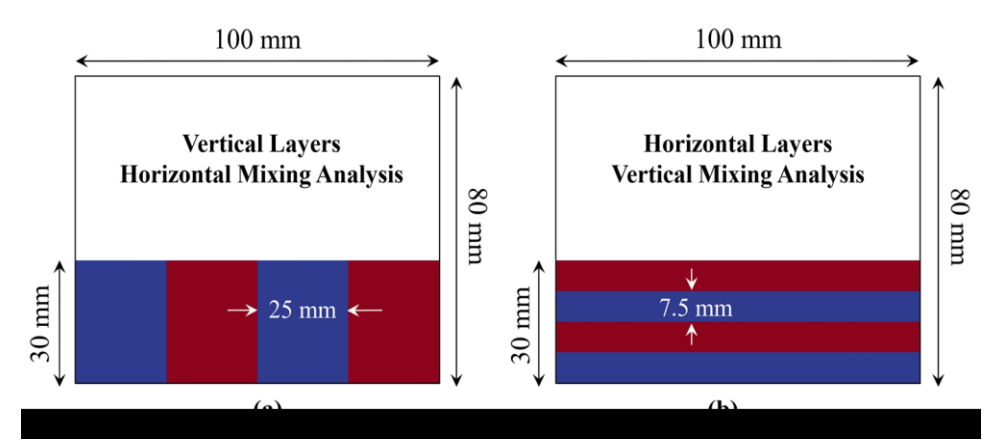


Figure 3. Schematic of the initial positions of the passive scalars used to assess (a) horizontal mixing and (b) vertical mixing.

3. Results and Discussion

3.1 Validation Against Experimental Results with Only Vertical Vibration

To validate the numerical simulation results, four cases with various bed heights (h_s) and with only vertical vibration were compared with the prior experimental data [15]. Prior data was only available in gas-fluidized beds with vertical vibration alone. The frequency of vibration was 10 Hz and superficial gas velocity was 1.04 U_{mf} . Table 2 presents the information of validation case setup.

Figure 4 presents a qualitative comparison between the results obtained from TFM simulations and experimental observations over the course of two vibration periods. This comparison specifically focuses on a case with a solids fill height of 35 mm. The graphical representation in Figure 4 demonstrates that the positions of wave crests and the fundamental characteristics of Faraday waves in TFM simulations closely resemble the experimental behavior. To facilitate a more comprehensive analysis, additional comparisons were conducted for four different bed heights, as depicted in Figure 5.

Figure 5(a) provides a quantitative assessment of the wavelength by comparing the results obtained from TFM simulations with the experimental data. The error bars in these plots indicate the standard deviation of the experimental measurements. Similarly, Figure 5(b) provides a comparison of wave heights between TFM simulations and experimental results. The numerical simulation error ranges for wavelength are reported to be between 2.23% and 7.35%, whereas for wave height, the error ranges between 5.96% and 10.05%. A detailed summary of these error ranges is available in Table 2.

Based on the comprehensive analysis conducted, the TFM simulations exhibit a strong agreement with the experimental results, as evidenced by the similarity in wave positions, main characteristics, and the overall consistency observed in the quantitative comparisons.

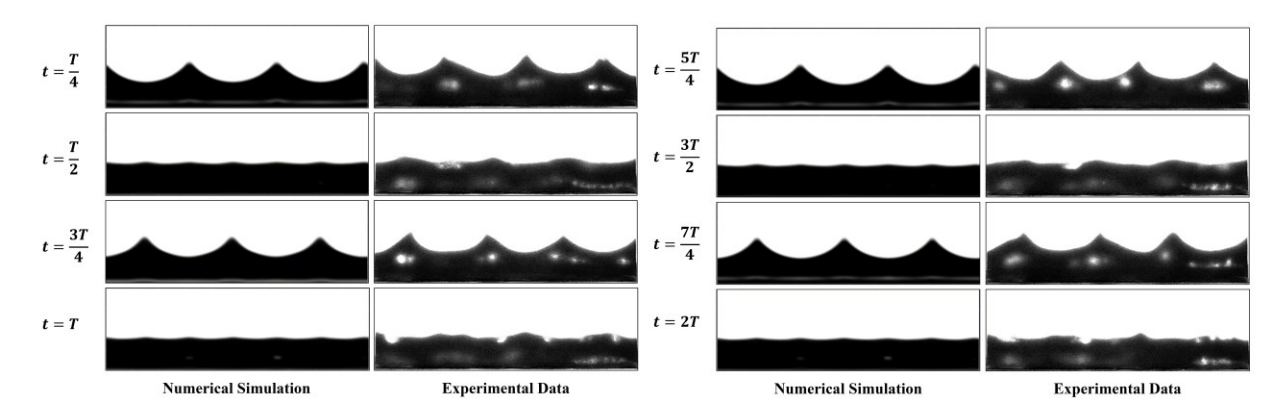


Figure 4. Time series of images of wave dynamics over the course of two vibration periods for experiments and simulations ($A_v = 2 \text{ mm}$, $f_v = 10 \text{ Hz}$, $\Gamma_v^* = 0.80$, $f_v^* = 5.9$, $U/U_{mf} = 1.04$, experimental $U_{mf} = 0.062 \text{ m/s}$, numerical $U_{mf} = 0.050 \text{ m/s}$, H = 35 mm).

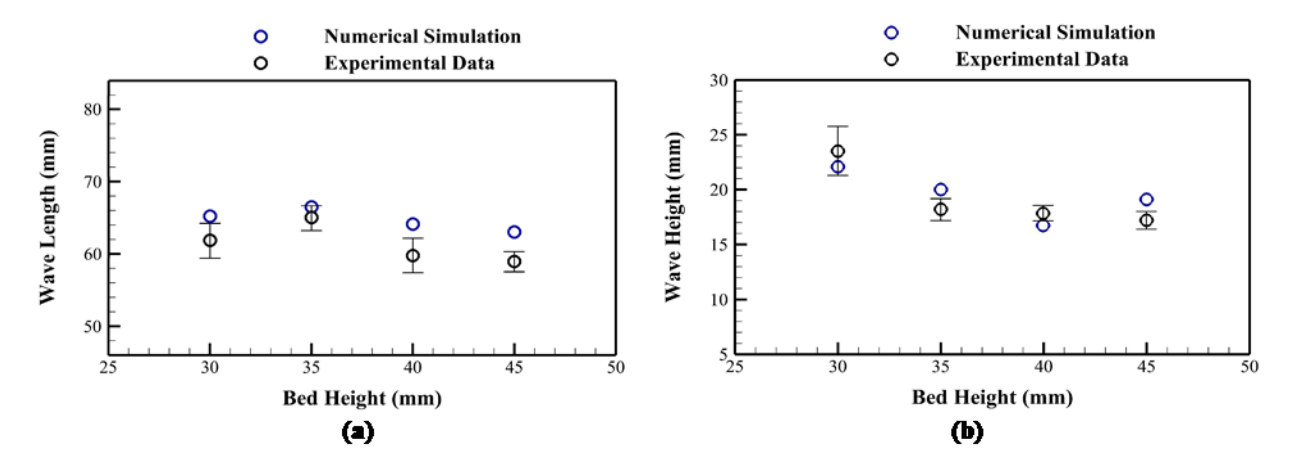


Figure 5. (a) Wavelength and (b) wave height vs. bed height from TFM simulations and experiments [6]; $A_v = 2$ mm, $f_v = 10$ Hz, $\Gamma_v^* = 0.80$, $U/U_{mf} = 1.04$.

Table 2. Validation case setup and comparison of wave properties with experimental results [6].

Exp. U_{mf} m/s	Num. U_{mf} m/s	f_v Hz	f _h Hz	$oldsymbol{d_{ss}}\ _{ m \mu m}$	$ ho_s$ kg/m ³	h _s	Wave length Num.	Wave length Exp.	Wave length Error	Wave Height Num. mm	Wave Height Exp. mm	Wave Height Error %
0.062	0.050	10	0	250	2500	30	65	62	5.4	2.2	2.4	5.96
0.062	0.050	10	0	250	2500	35	66	65	2.2	2.0	1.8	9.89
0.062	0.050	10	0	250	2500	40	64	60	7.4	0.94	1.1	9.48
0.062	0.050	10	0	250	2500	45	63	59	6.9	1.9	1.7	10.05

3.2 Faraday Wave Properties

3.2.1 Effects of Vertical and Horizontal Vibration Frequencies on Wave Dynamics

Here, we conduct a sensitivity analysis to examine the impact of horizontal and vertical vibration conditions on Faraday waves in gas-fluidized beds under bubble-free conditions, as depicted in Figure 6. In this subsection, bed height H = 30 mm, $A_h = 2$ mm, $A_v = 2$ mm and $U/U_{mf} = 1.04$. Figure 6(a) demonstrates that as the horizontal frequency increases from zero to 18 while maintaining a constant vertical frequency of 20 Hz, the wavelength increases. The wave height is not affected significantly by horizontal frequency.

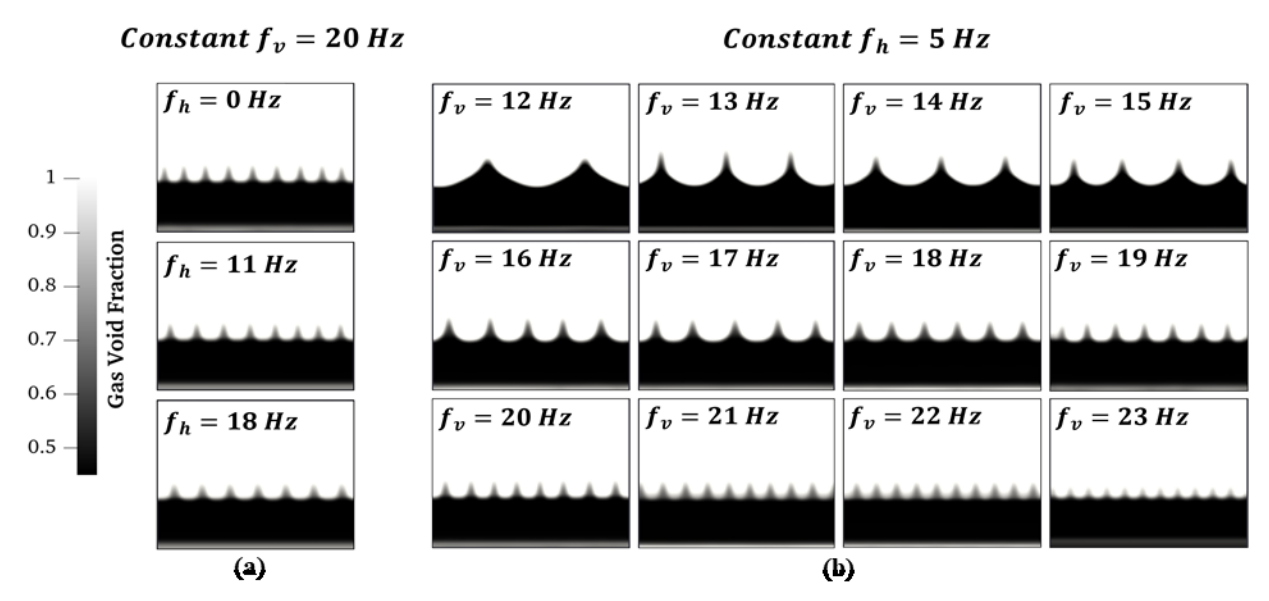


Figure 6. Images of wave dynamics formed with (a) varying horizontal vibration frequency and constant vertical vibration frequency $f_v = 20$ Hz and (b) varying vertical vibration frequency and constant horizontal vibration frequency $f_h = 5$ Hz ($A_h = 2$ mm, $A_v = 2$ mm, $U/U_{mf} = 1.04$, H = 30 mm).

In contrast, when the vertical frequency is increased from 12 to 23 Hz while maintaining a constant horizontal frequency of 5 Hz (Figure 6 (b)), as the vertical frequency increases, both wavelength and wave height decrease significantly. Thus, vertical frequency exerts a more dominant influence on wave dynamics than horizontal frequency.

The investigation of combined horizontal and vertical frequency effects was conducted over an extensive range of frequencies. Figure 7 presents two regime maps that provide comprehensive information on wavelength and wave height variations across different horizontal and vertical frequency values. The horizontal frequency ranges from 0 to 24 Hz, while the vertical frequency spans from 5 to 24 Hz. The vertical axis of the plot represents the vertical vibration strength, calculated using $\Gamma_v = 4\pi^2 f_v^2 A_v/g$, while the horizontal axis depicts the ratio of horizontal to vertical frequency, $f_r^* = f_h/f_v$. The color-coded regions in Figure 7 (a) and (b) correspond to wavelength and wave height values, respectively. Additionally, black points indicate instances where Faraday waves were not detectable in the system. In all cases shown in the regime maps, H = 30 mm, $A_v = 2$ mm, $A_h = 2$ mm and $U/U_{mf} = 1.04$.

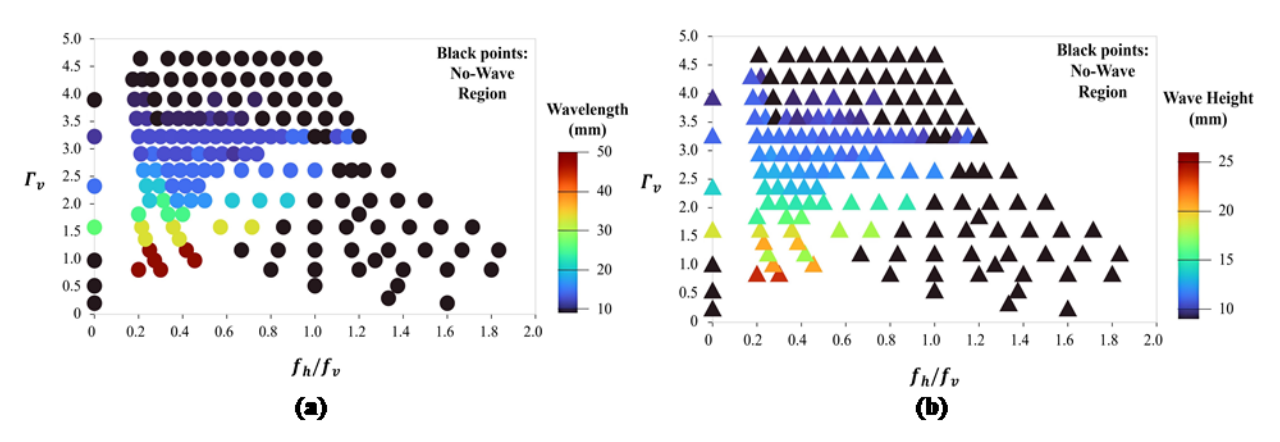


Figure 7. Regime map showing (a) wavelength and (b) wave height as a function of vertical vibration strength (Γ_v^*) and vibration frequency ratio (f_h/f_v) . $(A_h = 2 \text{ mm}, A_v = 2 \text{ mm}, U/U_{mf} = 1.04, H = 30 \text{ mm})$

As seen in Figure 7, with increasing vertical vibration strength, the wavelength and wave height decrease significantly. Increasing horizontal frequency also tends to decrease wavelength and wave height; however, the effects of horizontal vibration are much smaller than vertical vibration. Increasing horizontal vibration frequency tends to eliminate the formation of waves, particularly at high and low vertical vibration strengths. Vertical vibration strengths close to 3.0 create Faraday waves across the widest range of horizontal vibration conditions.

3.2.2 Effects of Gas Velocity on Wave Dynamics

Here, we investigate influence of superficial gas velocity on wave dynamics. Figure 8 displays the structured Faraday waves under two distinct conditions for five values of U/U_{mf} , namely 0, 0.5, 1.0, 1.5, and 2.0. The first condition involves only vertical vibration in the system (Figure 8 (a)), while the other represents a combination of horizontal and vertical vibrations (Figure 8 (b)). For this investigation, the horizontal and vertical frequencies were set at 5 Hz and 16 Hz, respectively. The bed height is H = 30 mm, $A_h = 2$ mm and $A_v = 2$ mm.

In the absence of gas flow with only vertical vibration, the crest of the waves exhibits bending, and the wavelengths are unevenly distributed. However, upon adding horizontal vibration, even without gas flow, the wave shapes are no longer bent, and the wavelengths become equal. With only vertical vibration, introducing gas flow also acts to straighten the waves formed. In both cases with only vertical vibration and combined horizontal and vertical vibration, increasing gas flow increases the wavelength.

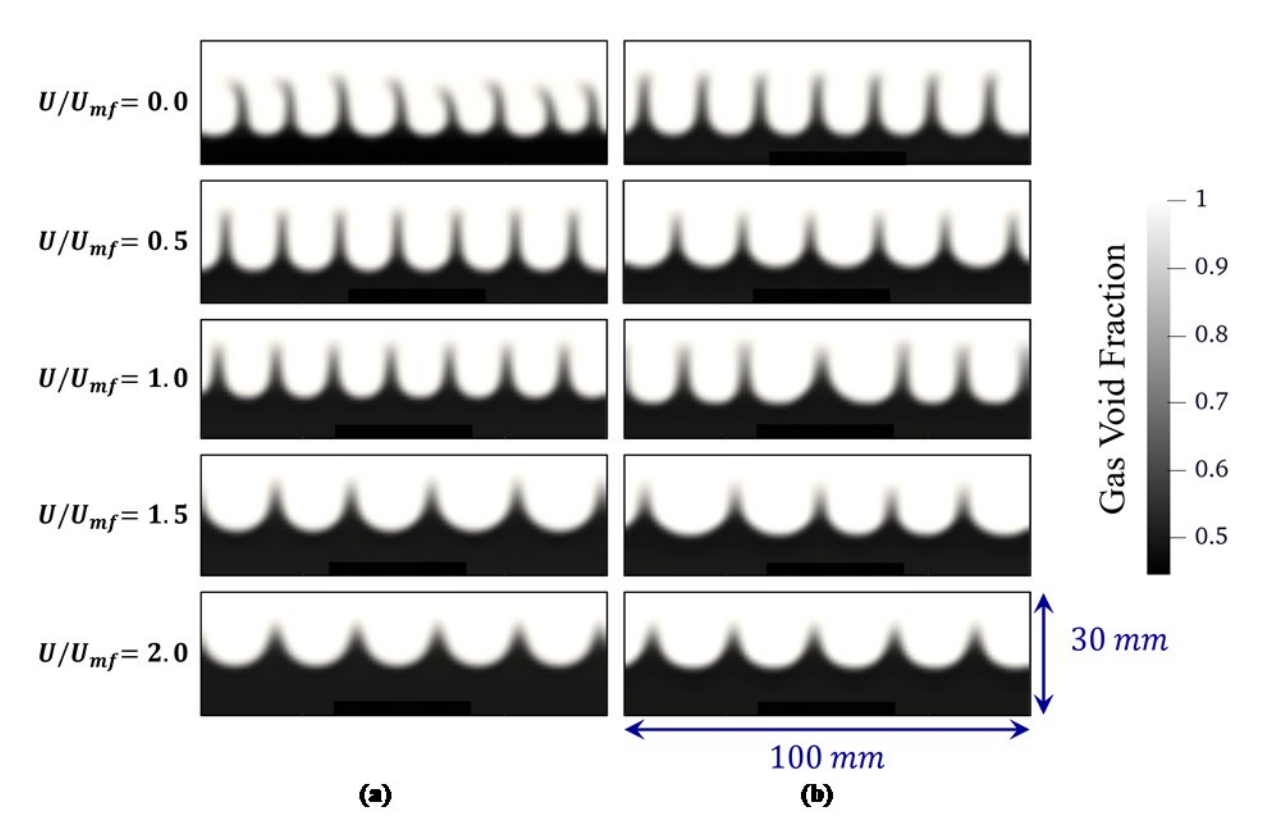


Figure 8. Images of wave dynamics formed with varying U/U_{mf} for (a) only vertical vibration and (b) combined vertical and horizontal vibration ($A_h = 2 \text{ mm}$, $A_v = 2 \text{ mm}$, $f_h = 5 \text{ Hz}$, $f_v = 16 \text{ Hz}$, H = 30 mm, $\Gamma_v^* = 2.1$, $f_v^* = 8.7$)

3.2.3 Dimensional Analysis for Predicting Wavelength and Wave Height

Here, we conduct Buckingham-Pi dimensional analysis [40] to develop non-dimensional correlations for predicting wavelength and wave height, based on dimensional input parameters summarized in Table 3. There are 13 total dimensional parameters (4 material properties, 7 input parameters and 2 output parameters) and 3 dimensions (mass, length and time), and thus 10 non-dimensional parameters are needed to describe the system. As such we have chosen 10 non-dimensional parameters to describe the system, largely based on prior studies [6,11,41,42], determining their importance for capturing dynamics in gas fluidized beds and vibrated grains.

Table 3. Dimensional analysis for correlating wavelength and wave height to known parameters,

based on material properties and input parameters.

Material	Unit	Input	Unit	Output	Unit	Problem	Dimensionless	Equation
Property		Parameter		Parameter		Dimension	Group	
Particle	m	Gravitational	m s ⁻²	Wavelength,	m	Mass (kg)	Particle Reynolds	$Re_s^* =$
diameter,		acceleration,		λ			Number, Re_s^*	$ ho_g U d_s \mu^{-1}$
$\underline{}$ d_s		g						
Particle	kg m⁻	Particle bed	m	Wave height,	m	Length (m)	Archimedes	$Ar^* =$
density,	3	height, H		λ_V			Number, Ar^*	$(ho_s- ho_g)$
$ ho_s$								$\rho_g d_s^3 \mu^{-2}$
Gas density,	kg m ⁻	Superficial gas velocity,				Time (s)	Normalized frequency, f_v^*	$f_v H^{1/2} g^{-1/2}$
$ ho_g$		U						
Gas viscosity, μ	kg m s ⁻¹	Vertical vibration amplitude, A_v					Vertical Vibration Strength, Γ_{v}^{*}	$4\pi^2 A_v f_v^2 g^{-1}$
<u>µ</u>		Vibration frequency, f_v					Strouhal Number, Str*	$f_v A_v U^{-1}$
		Horizontal vibration amplitude, A_h					Frequency Ratio, f_r^*	$f_h f_v^{-1}$
		Horizontal frequency, f_h					Amplitude Ratio, A_r^*	$A_h A_v^{-1}$
							Horizontal Vibration Strength, Γ_h^*	$4\pi^2 A_h f_h^2 g^{-1}$
							λ^*	$\lambda f_v^2 g^{-1}$
							λ_{v}^{*}	$\lambda_{\nu}\lambda^{-1}$
Total: 4		Total: 7		Total: 2		Total: 3	Total: 10	Max. Needed: 10

Based on the chosen parameters, we developed the following non-dimensional correlations to predict wavelength and wave height based on parameters known *a priori*:

$$\lambda^* = c_h R e_s^{*c_{1,h}} A r^{*c_{2,h}} f_v^{*c_{3,h}} \Gamma_v^{*c_{4,h}} S t r^{*c_{5,h}} f_r^{*c_{6,h}} A_r^{*c_{7,h}} \Gamma_h^{*c_{8,h}}$$
(21)

$$\lambda_{v}^{*} = c_{v} R e_{s}^{*c_{1,v}} A r^{*c_{2,v}} f_{v}^{*c_{3,v}} \Gamma_{v}^{*c_{4,v}} S t r^{*c_{5,v}} f_{r}^{*c_{6,v}} A_{r}^{*c_{7,v}} \Gamma_{h}^{*c_{8,v}}$$

$$(22)$$

In the above equations, the c values are fitted by comparison with the numerical simulation data using least squares regression. Least squares regression was performed between c values of -5 to 5 in increments of 1. More precise least squares regression was performed on the optimum c values to obtain better agreement to numerical simulation data; for this, increments were one order of magnitude less than the previous least squares regression (0.1) and the range was half the value of the previous least squares regression (± 0.5) . This method was repeated, with decreasing increment size, until the difference between the sum of squares for the previous least squares regression and current least squares regression was less than 1%. The values yielded from this are shown in Table 4. Using the c values in Table 4, the predicted values of dimensional and non-dimensional wavelength and wave height are shown in Figure 9. Values for $c_{7,h}$ and $c_{7,v}$ were not fitted because A_r^* has a value of $A_r^* = 1$ for all investigated parameters in the numerical study.

Table 4. Non-dimensional correlation values for Equations (21) and (22) based on least squared fitting from of the simulation data with varying vibration and gas flow conditions.

Wavelength Constant	Value	Wave Height Constant	Value
c_h	2.54	c_v	1.70
$c_{1,h}$	-4.33	$c_{1,v}$	-5.47
$c_{2,h}$	-1.10	$c_{2,v}$	-0.99
$c_{3,h}$	-4.49	$c_{3,v}$	-1.51
$c_{4,h}$	3.28	$c_{4,v}$	1.66
$c_{5,h}$	-4.44	$c_{5,v}$	-5.17
$c_{6,h}$	-1.99	$c_{6,v}$	-4.49
$c_{7,h}$	-	$c_{7,v}$	-
c _{8,h}	1.01	$c_{8,v}$	2.21

Figure 9 shows that the values of dimensional and non-dimensional wavelength and wave height obtained from the least squares method are comparable to those obtained from the numerical simulations. The values from the least squares method are a good match to the values from the simulations at small wavelength and wave height, where the simulation data is most concentrated. A fair match is obtained for specific cases at high wavelength and wave height. The difference between the values from the least squares method and simulations is small for all varying conditions. Thus, the accuracy of the model is independent of which conditions are varied. The mean difference between values for wavelength and wave height from the least squares model and simulations was found to be 9.5% and 8.0%, respectively. The good agreement between the values from the least squares model and the values from the simulations suggests that the model may be applicable for other systems at different conditions.

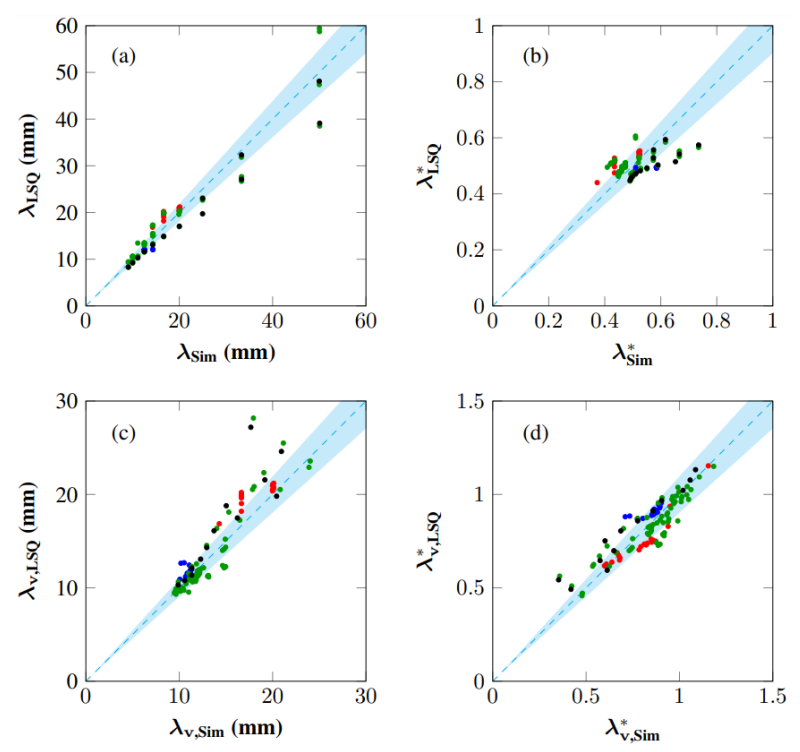


Figure 9. Value from simulations vs. value predicted by correlations (Equations (21) and (22)) for (a,c) dimensional and (b,d) non-dimensional (a,b) wavelength and (c,d) wave height for varying vibration and gas flow conditions. The plot markers represent (\bullet) varying vertical vibration strength, Γ_v^* (constant Γ_h^* , U^*), (\bullet) varying horizontal vibration strength, Γ_h^* (constant Γ_v^* , U^*), (\bullet) varying gas velocity, U^* (constant Γ_v^* , Γ_h^*), and (\bullet) varying all three main parameters (Γ_v^* , Γ_h^* , U^*). The line of equality between simulated values as regression values is given by (---). The shaded region in each plot shows the \pm 10% error region.

3.2.4 Effect of Relative Vertical and Horizontal Vibration Phase on Wave Dynamics

Here, we explore the effects of phase offset between horizontal and vertical vibrations on Faraday wave patterns. By analyzing various phase offsets and comparing the results to the inphase condition, we aim to gain insights into the behavior of these patterns. The numerical setup includes a bed with a height of 30 mm and applied horizontal and vertical frequencies of 17 Hz. Additionally, a superficial gas velocity of 1.04 U_{mf} was maintained. To examine the impact of phase offset, we employed three different phase settings: $\pi/4$, $\pi/2$, and π ($\overline{g_h} = (2\pi f_h)^2 A_h \sin(2\pi f_h(t+\tau))$ in which τ is phase offset), in addition to the in-phase condition. The comparison was performed for two periods of wave stationary displacement, as depicted in Figure 10.

The comparison illustrated in Figure 10 reveals differences when phase offsets are introduced into the system. For most cases, there are 6 waves in the system, yet for the fully out-of-phase condition, the wavelength increases and there are 5 waves in the system.

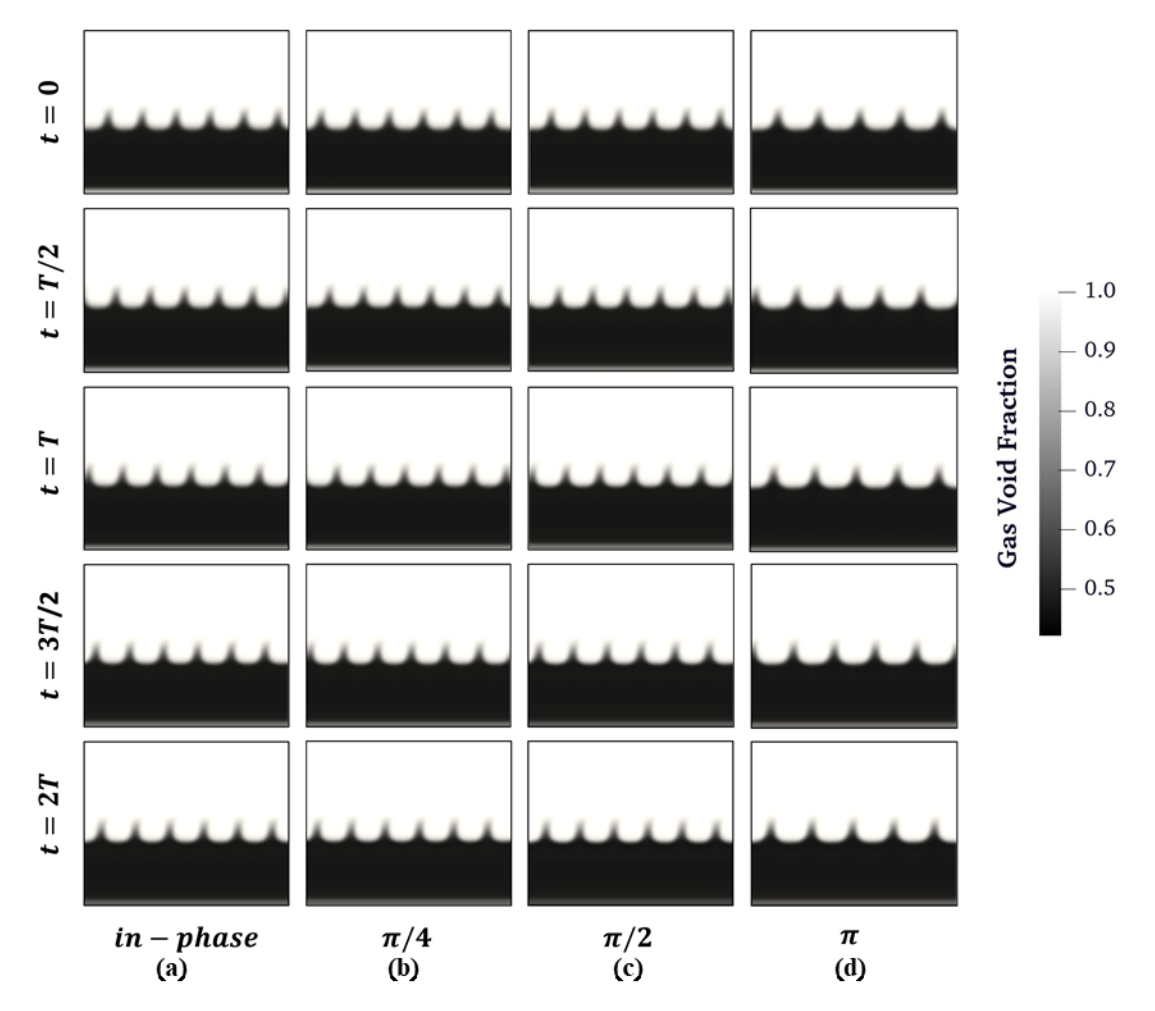


Figure 10. Time series of images of wave dynamics over the course of two vibration periods for (a) vertical and horizontal vibration in-phase, (b) $\pi/4$ out-of-phase, (c) $\pi/2$ out-of-phase, and (d) π out-of-phase; ($A_h = A_v = 2$ mm, $f_h = f_v = 17$ Hz, $U/U_{mf} = 1.04$, H = 30 mm, $\Gamma_v^* = 2.1$, $f_v^* = 2.3$).

3.2.5 Dynamics with Only Horizontal Vibration

In this section, by exclusively applying horizontal vibration and simulating various cases using the TFM model, the impact of only horizontal vibration on the patterns of granular flow is analyzed. Figure 11 presents the results of these simulations, showcasing two-period time series for four different horizontal frequencies: 5, 10, 15, and 20 Hz. The vibration amplitude for this study was set to 2 mm, and the superficial gas velocity was maintained at $1.04\ U_{mf}$.

Figure 11 highlights the absence of Faraday waves in the system when only horizontal vibration is applied. Despite varying the amplitude from 2 to 5 and 10 mm, no discernible impact on the appearance of these patterns was observed. Similarly, increasing the superficial gas velocity ratio from 1.04 to 1.5 and 2.0 yielded no observable effect on the presence of Faraday waves within the system. The absence of Faraday waves in the system when subjected solely to horizontal vibration indicates that other factors, such as vertical vibrations, play a crucial role in their

formation. These results can be explained by the particle bed needing to leave the base of the system and then impact with the base periodically to produce waves.

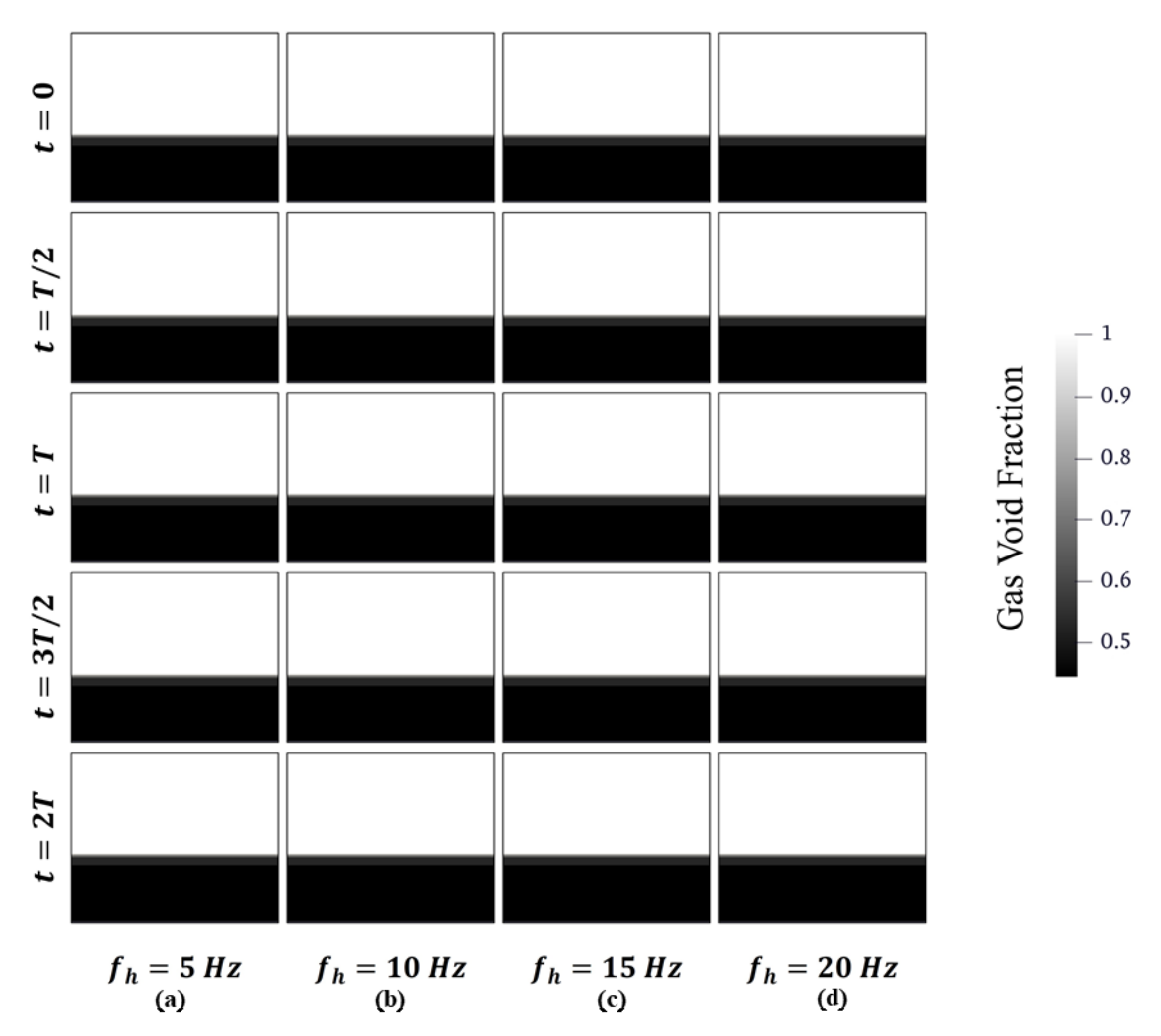


Figure 11. Time series of images of wave dynamics over the course of two vibration periods for different horizontal frequencies with no vertical vibration ($A_h = 2 \text{ mm}$, $U/U_{mf} = 1.04$, H = 30 mm).

3.3 Particle Mixing

3.3.1 Effect of Vibration Conditions on Mixing

Here, we examine the influence of horizontal and vertical frequencies on the degree of mixing within the system over time. Figure 12 presents a time series of mixing contours in the fluidized bed during the initial 30 seconds, with horizontal frequencies of 0, 5, 10, and 15 Hz, while maintaining a constant vertical frequency of 20 Hz. Notably, Figure 12 (a) demonstrates that changes in horizontal frequency have minimal impact on the vertical mixing. However, an increase in horizontal frequency has a considerable effect on mixing in the horizontal direction, speeding up the rate of horizontal mixing with increasing horizontal frequency.

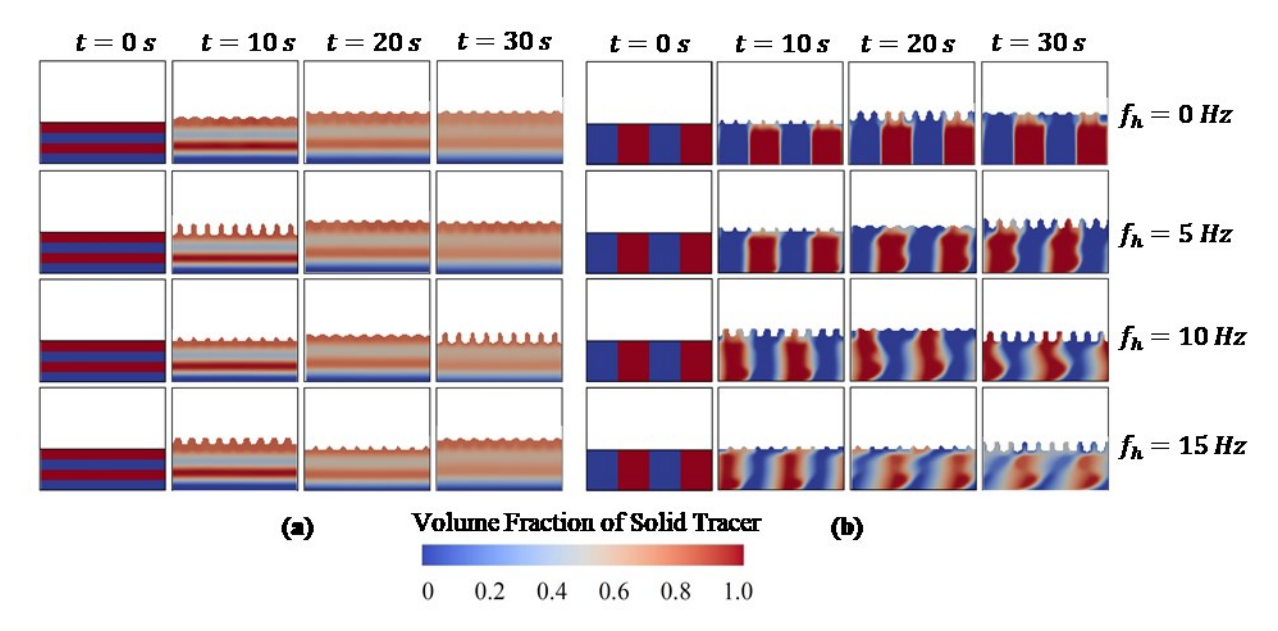


Figure 12. Time series of images of mixing dynamics formed with varying horizontal vibration frequency and constant vertical vibration frequency $f_v = 20$ Hz for (a) vertical mixing and (b) horizontal mixing $(A_h = 2 \text{ mm}, A_v = 2 \text{ mm}, U/U_{mf} = 1.04, H = 30 \text{ mm}, \Gamma_v^* = 3.2)$.

An analogous analysis was conducted, considering changes in vertical frequencies of 0, 13, 15, and 18 Hz, while maintaining a constant horizontal frequency of 5 Hz. Figure 13 depicts the time series of mixing contours for these cases, representing various particle layers in both horizontal and vertical directions. In Figure 13, where only horizontal vibration is applied ($f_v = 0$), mixing in the vertical direction maintains a consistent shape over time, while some degree of mixing is observed in the horizontal direction. However, this mixing is notably weaker compared to the combined horizontal and vertical vibration case, indicating that horizontal vibration alone is not effective for generating mixing in the system. Incorporating vertical vibration is essential to fully observe the impact of horizontal vibration. As vertical frequencies increase from 13 Hz to 18 Hz, a reduction in mixing occurs, suggesting that lower vertical frequencies result in more efficient mixing in the fluidized bed system. This reduction in mixing at high vertical frequencies is likely due to the wavelength and wave height decreasing at high vertical frequencies.

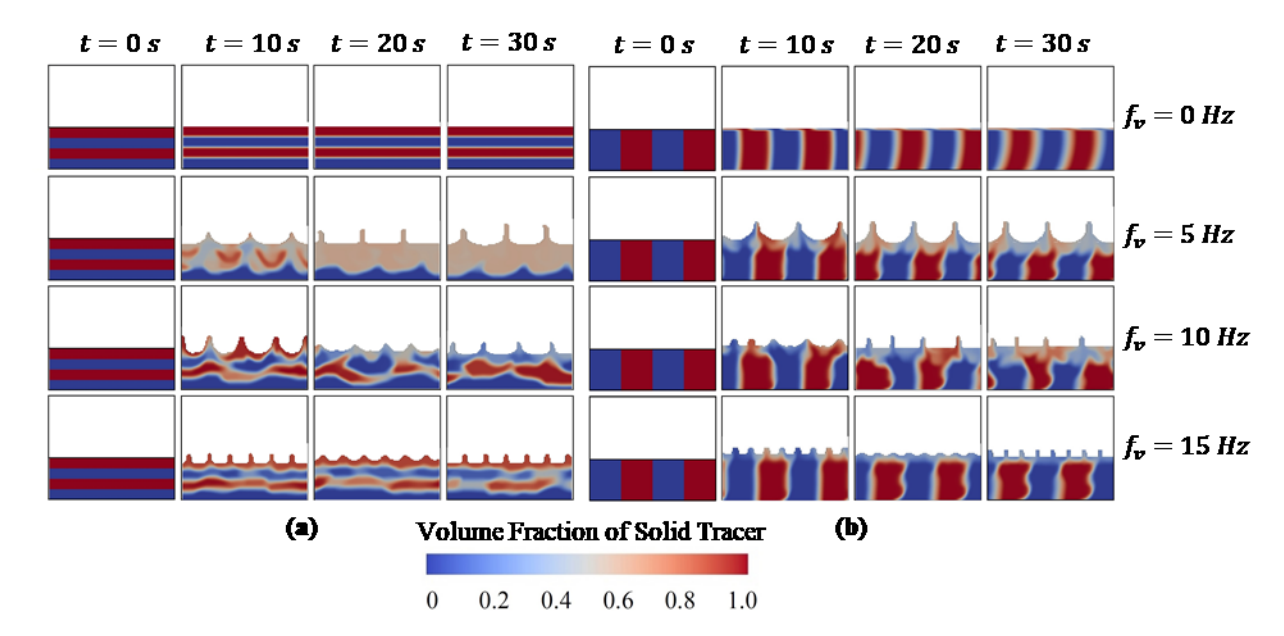


Figure 13. Time series of images of mixing dynamics formed with varying vertical vibration frequency and constant horizontal vibration frequency $f_h = 5$ Hz for (a) vertical mixing and (b) horizontal mixing; $(A_h = 2 \text{ mm}, A_v = 2 \text{ mm}, U/U_{mf} = 1.04, H = 30 \text{ mm})$.

For the quantification of mixing results, segregation intensity was utilized, calculated according to Equation (18). In this section, first three cases of (i) gas flow only, (ii) vertical vibration with gas flow, and (iii) combined horizontal and vertical vibration with gas flow are compared. The simulations were conducted with a gas velocity 1.04 U_{mf} , while keeping the horizontal and vertical frequencies fixed at 10 Hz. Figure 14 show these quantitative mixing results.

In Figure 14 (a), focused on mixing analysis in the horizontal direction, the case with gas flow alone exhibits no significant effect on mixing, resulting in a constant segregation intensity value of 1. Comparatively, the case with only vertical vibration demonstrates a similar degree of mixing to the case of combined horizontal and vertical vibrations, albeit with a slightly slower rate. Thus, the introduction of horizontal vibration to the system accelerates the mixing process, leading to more accurate and expedited mixing outcomes in comparison to the case with only vertical vibration. Furthermore, Figure 14 (b) reveals a substantial effect of adding horizontal vibration to the system for mixing in the horizontal direction. Notably, vertical vibration alone is insufficient to achieve effective mixing of particles in the horizontal direction. These findings emphasize the significant role played by combined horizontal and vertical vibrations in enhancing mixing efficiency within the fluidized bed system.

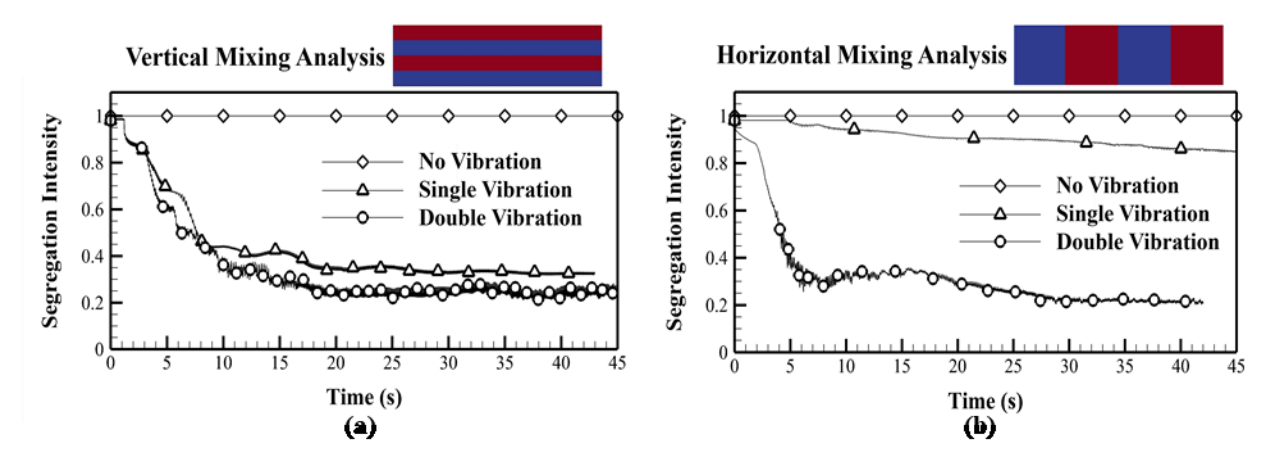


Figure 14. Segregation intensity vs. time for (i) no vibration (only gas flow), (ii) only vertical vibration and (iii) combined vertical and horizontal vibration for (a) vertical mixing and (b) horizontal mixing; ($A_h = 2 \text{ mm}$, $A_v = 2 \text{ mm}$, $f_h = 10 \text{ Hz}$, $f_v = 10 \text{ Hz}$, $U/U_{mf} = 1.04$, H = 30 mm, $\Gamma_v^* = 0.80$, $f_v^* = 5.4$).

Figure 15 provides a comprehensive quantification of the cases depicted in Figures 12 and 13, allowing a detailed examination of the effects of horizontal and vertical vibrations on the mixing. In Figure 15 (a), with a constant vertical frequency of 20 Hz, increasing the horizontal frequency from 0 to 15 does not yield noticeable changes in the rate of mixing in the vertical direction. However, in the horizontal direction (Figure 15 (b)), increasing horizontal vibration frequency significantly increases horizontal mixing rate.

Furthermore, the analysis reveals that increasing vertical vibration frequency with a constant horizontal frequency decreases the rate and extent of mixing in both the horizontal and vertical directions (Figure 15 (c) & (d)). These findings emphasize the crucial role of combined horizontal and vertical vibrations in enhancing mixing efficiency in the fluidized bed system, particularly in the horizontal direction. Additionally, they highlight the sensitivity of the mixing process to variations in vertical vibration, underscoring the need for careful consideration of both horizontal and vertical frequency settings to optimize mixing performance in practical applications.

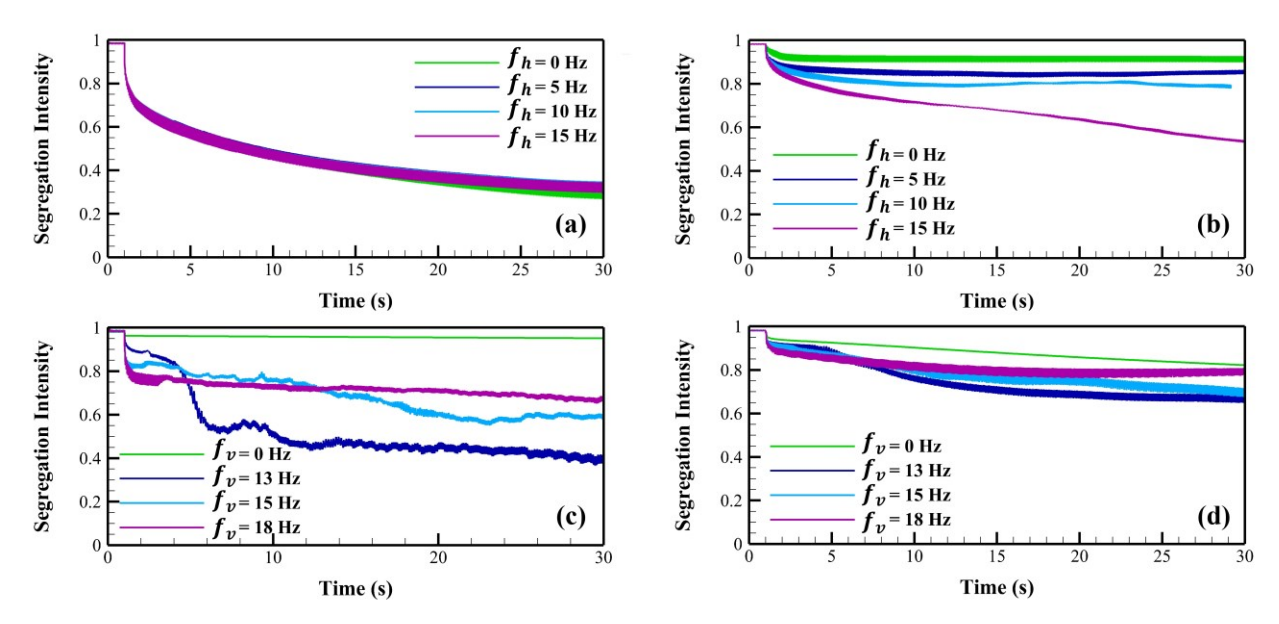


Figure 15. Segregation intensity vs. time for (a,b) varying horizontal vibration frequency and constant vertical vibration frequency $f_v = 20$ Hz and (c,d) varying vertical vibration frequency and constant horizontal vibration frequency $f_h = 5$ Hz for (a,c) vertical mixing and (b,d) horizontal mixing ($A_h = 2$ mm, $A_v = 2$ mm, $U/U_{mf} = 1.04$, H = 30 mm).

3.3.2 Effect of Gas Velocity on Mixing

To examine the effects of gas flow velocity on the mixing rate and extent, four U/U_{mf} velocity ratios of 0.5, 1.0, 1.5, and 2.0 were selected for analysis. Figure 16 displays the time series mixing images for these cases, considering both only vertical vibration and the combination of horizontal and vertical vibrations. The quantification of these cases is further depicted as segregation intensity plots in Figure 17.

In Figure 16 (a) and Figure 17 (a), it is evident that for mixing in the vertical direction with only vertical vibration, increasing the velocity ratio up to 1.5 results in incremental increases in mixing, but beyond that point, further increasing the gas velocity has a negative effect on mixing. However, the final mixing condition at the gas velocity ratio of 2.0 still outperforms the ratio of 1.0. When horizontal vibration is applied in this scenario (Figures 16 (c) and 17 (c)), it becomes apparent that the best velocity ratio for mixing is 0.5, which closely approximates the mixing results of the ratios 1.0 and 1.5. This observation confirms that incorporating horizontal vibration compensates for the gas velocity's impact on mixing in the fluidized bed. Consequently, adding horizontal vibration can enhance the mixing efficiency in the system, offering a promising strategy to mitigate the adverse effects of gas flow velocity and optimize mixing performance.

In the cases of mixing in the horizontal direction, increasing the gas velocity negatively impacted mixing for both scenarios of only vertical and combined vibrations (Figures 16 (b) & (d) and 17 (b) & (d)). Additionally, with the inclusion of horizontal vibration, a case with a velocity ratio of 1.0 achieved a better mixing rate as compared to the case with a ratio of 1.5 in the only vertically vibrated scenario. This finding further supports the notion that by adding horizontal

vibration, we can attain a specific mixing degree in the fluidized bed with lower gas velocities. In essence, horizontal vibration acts as a compensating factor, enabling the system to achieve desired mixing efficiency with reduced gas flow velocities.

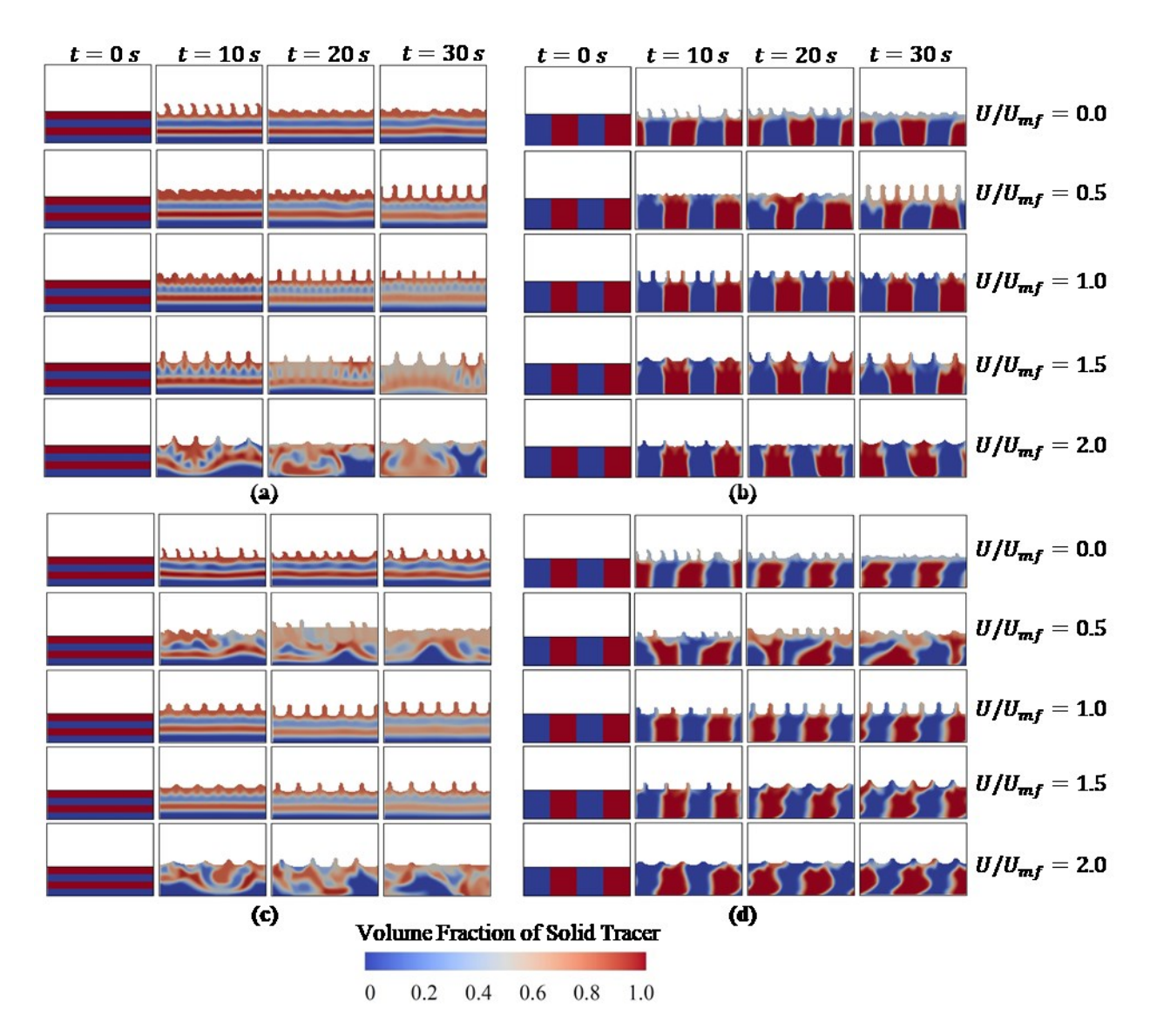


Figure 16. Time series of images of mixing dynamics formed with varying U/U_{mf} for (a,c) vertical mixing and (b,d) horizontal mixing for (a,b) only vertical vibration and (c,d) combined vertical and horizontal vibration; ($A_h = 2 \text{ mm}$, $A_v = 2 \text{ mm}$, $f_h = 5 \text{ Hz}$, $f_v = 16 \text{ Hz}$, $f_v = 30 \text{ mm}$, $f_v = 2.1$, $f_v = 8.7$).

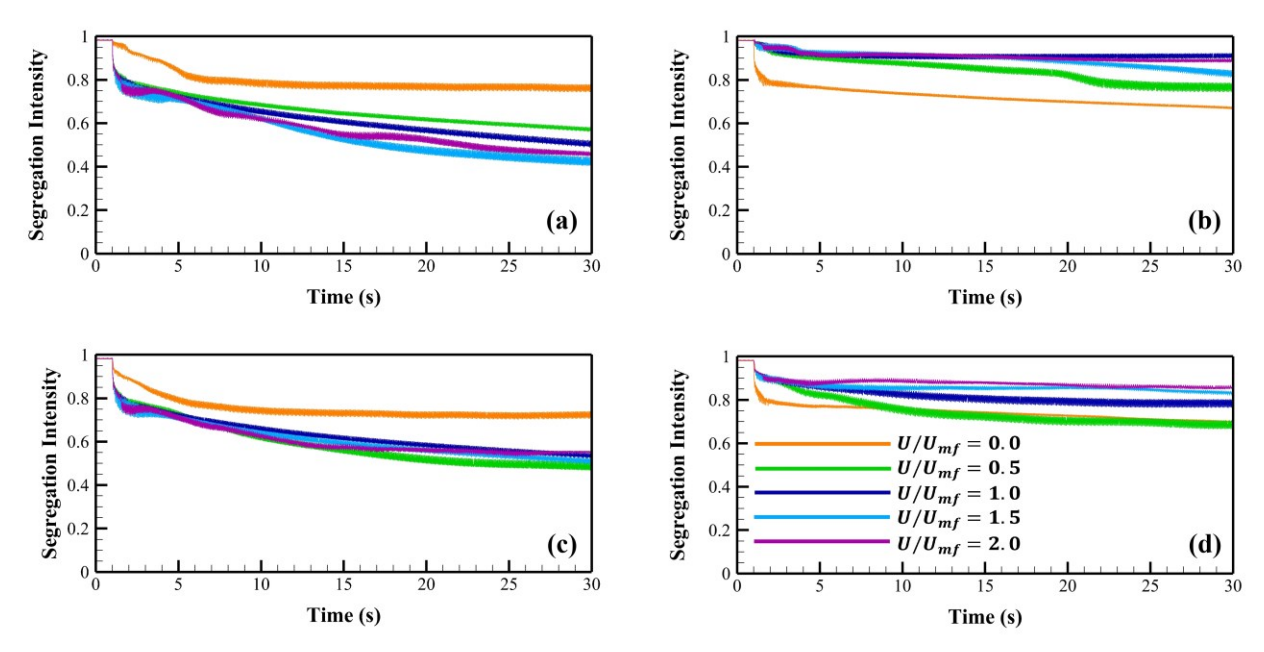


Figure 17. Segregation intensity vs. time formed with varying U/U_{mf} for (a,c) vertical mixing and (b,d) horizontal mixing for (a,b) only vertical vibration and (c,d) combined vertical and horizontal vibration; ($A_h = 2 \text{ mm}$, $A_v = 2 \text{ mm}$, $f_h = 5 \text{ Hz}$, $f_v = 16 \text{ Hz}$, H = 30 mm, $\Gamma_v^* = 2.1$, $f_v^* = 8.7$).

4. Conclusion

In this work, we investigated the effect of combined horizontal and vertical vibration on Faraday wave dynamics and particle mixing in vibrated gas-fluidized beds. Prior studies have only involved vertical vibration of gas-fluidized beds to produce Faraday waves, and here we investigated combined vertical and horizontal vibration using TFM simulations. The key physical insight from this study is that adding horizontal vibration to gas flow and vertical vibration in fluidized beds can maintain Faraday waves while significantly increasing rates of horizontal mixing.

Further, this study parametrically characterizes the effects of varying gas flow, vertical vibration and horizontal vibration conditions. Increasing vertical vibration frequency significantly decreases wavelength and wave height, while varying horizontal frequency has less of an impact on wave dynamics. Increasing gas flow rate increases wavelength while decreasing wave height. Regime maps and dimensionless correlations are formed to guide the effects of vibration and gas flow conditions on wave properties. We further demonstrate that horizontal vibration on its own cannot create surface waves, and introducing a phase offset between horizontal and vertical vibration has minor effects on wave dynamics. Horizontal and vertical mixing were also investigated under various gas flow and vibration conditions. Adding horizontal vibration to vertical vibration significantly increases mixing, particularly in the horizontal direction. Mixing rate is optimized at low vertical frequencies, high horizontal frequencies and low normalized gas velocities.

The insights from this study inspire a number of future studies. The fast rate of mixing of particles while maintaining Faraday waves motivates the application of combined vibration to

processes which could benefit from this flow behavior, such as highly exothermic reactors and pharmaceutical mixers. Further, the insights from TFM simulations can be validated by experimental studies, and more detailed simulations studies can investigate the physical mechanisms underlying the flow patterns observed here. Finally, experimental and simulation studies can be conducted to investigate how the combination of vertical and horizontal vibration impacts flow dynamics in fully 3D gas-fluidized beds.

Nomenclature

ε	Volume fraction	λ_v	Wave height, m
ρ	Density, kg/m^3	Str^*	Strouhal number
\vec{u}	Velocity, <i>m/s</i>	Re^*	Reynolds number
p	Pressure, Pa	Ar^*	Archimedes number
μ	Viscosity, $Pa \cdot s$	$ec{g}$	Gravitational acceleration, m/s^2
$ar{ar{ au}}$	Stress tensor, Pa	Γ	Vibration strength
$\varepsilon_{s,max}$	Packing limit	t	Time, s
$\varepsilon_{s,minf}$	Critical solids concentration	U_{mf}	Minimum fluidization velocity, m/s
d_s	Particle size of the solids phase, m	U	Superficial gas velocity, m/s
p_c	Solids pressure at a critical state, Pa	V_{cell}	Volume of a CFD cell, m^3
$\chi_{_S}$	Mass fraction of the tracer in the solids phase	$V_{particle}$	Volume of a particle, m^3
m	Mass of the solids phase, kg	$\sigma(x_S)$	Standard deviation of the mass fraction of tracer particles present in all CFD cells
S_a	Surface area of the solids phase, m^2	N_{tracer}	Total number of tracer particles in the system
	Momentum exchange coefficient		Total symbon of all mostial as museout
β	between the gas phase and the solids phase, $kg/(m^3 \cdot s)$	N_{total}	Total number of all particles present in the system
C_D	Drag coefficient	SI	Segregation intensity
Re	Reynolds number	Subscript	
ϕ	Angle of internal friction, °	g	Gas phase
$\overline{\overline{S}}$	Deviatoric rate-of-strain tensor of the solids phase	S	Solids phase
$ar{ar{I}}$	Identity tensor	h	Horizontal Vibration
\boldsymbol{A}	Vibration amplitude, m	v	Vertical Vibration
f	Vibration frequency, Hz	Superscript	
c_h	Wavelength constant	k	Kinetic contributions to the solids stress
c_v	Wave height constant	f	Frictional contributions to the solids stress
Н	Particle bed height, m	*	Normalized value
λ	Wavelength, m		

Acknowledgements

This work was financially supported by Office of Naval Research grant N00014-23-1-2041 and National Science Foundation grant 2144763.

References

- [1] J.F. Davidson, D. Harrison, Fluidised Particles, Cambridge University Press, Cambridge, 1963.
- [2] G. D'Anna, P. Mayor, A. Barrat, V. Loreto, F. Nori, Observing brownian motion in vibration-fluidized granular matter, Nature 424 (2003) 909–912. https://doi.org/10.1038/nature01867.
- [3] H.K. Pak, P.R. Behringer, Bubbling in vertically vibrated granular materials, Nature 371 (1994) 231–233. https://doi.org/10.1038/371231a0.
- [4] C.R. Wassgren, C.E. Brennen, M.L. Hunt, Vertical Vibration of a Deep Bed of Granular Material in a Container, Journal of Applied Mechanics 63 (1996) 712–719. https://doi.org/10.1115/1.2823354.
- [5] L. de Martín, C. Ottevanger, J.R. van Ommen, M.-O. Coppens, Universal stability curve for pattern formation in pulsed gas-solid fluidized beds of sandlike particles, Phys. Rev. Fluids 3 (2018) 034303. https://doi.org/10.1103/PhysRevFluids.3.034303.
- [6] C. Bizon, M.D. Shattuck, J.R. de Bruyn, J.B. Swift, W.D. McCormick, H.L. Swinney, Convection and Diffusion in Patterns in Oscillated Granular Media, Journal of Statistical Physics 93 (1998) 449–465. https://doi.org/10.1023/B:JOSS.0000033158.05927.3f.
- [7] L.A. Vandewalle, V. Francia, K.M. Van Geem, G.B. Marin, M.-O. Coppens, Solids lateral mixing and compartmentalization in dynamically structured gas—solid fluidized beds, Chemical Engineering Journal 430 (2022) 133063. https://doi.org/10.1016/j.cej.2021.133063.
- [8] J. Li, I.S. Aranson, W.-K. Kwok, L.S. Tsimring, Periodic and Disordered Structures in a Modulated Gas-Driven Granular Layer, Phys. Rev. Lett. 90 (2003) 134301. https://doi.org/10.1103/PhysRevLett.90.134301.
- [9] R. Moosavi, M. Maleki, M.R. Shaebani, J.C. Ruiz-Suárez, E. Clément, Stripe formation in horizontally oscillating granular suspensions, EPL 107 (2014) 34006. https://doi.org/10.1209/0295-5075/107/34006.
- [10] E. Cerda, F. Melo, S. Rica, Model for Subharmonic Waves in Granular Materials, Phys. Rev. Lett. 79 (1997) 4570–4573. https://doi.org/10.1103/PhysRevLett.79.4570.
- [11] F. Melo, P. Umbanhowar, H.L. Swinney, Transition to parametric wave patterns in a vertically oscillated granular layer, Phys. Rev. Lett. 72 (1994) 172–175. https://doi.org/10.1103/PhysRevLett.72.172.
- [12] M.O. Coppens, J.R. van Ommen, Structuring chaotic fluidized beds, Chemical Engineering Journal 96 (2003) 117–124. https://doi.org/10.1016/j.cej.2003.08.007.
- [13] E.W. Merrow, Linking R&D to Problems Experienced in Solids Processing, (1984).
- [14] Q. Guo, Y. Zhang, A. Padash, K. Xi, T.M. Kovar, C.M. Boyce, Dynamically structured bubbling in vibrated gas-fluidized granular materials, PNAS 118 (2021). https://doi.org/10.1073/pnas.2108647118.
- [15] Q. Guo, W. Da, R. Wu, Y. Zhang, J. Wei, C.M. Boyce, Faraday wave instability analog in vibrated gas-fluidized granular particles, Phys. Rev. E 107 (2023) 034603. https://doi.org/10.1103/PhysRevE.107.034603.
- [16] S.E. Lehmann, E.-U. Hartge, A. Jongsma, I.-M. deLeeuw, F. Innings, S. Heinrich, Fluidization characteristics of cohesive powders in vibrated fluidized bed drying at low vibration frequencies, Powder Technology 357 (2019) 54–63. https://doi.org/10.1016/j.powtec.2019.08.105.
- [17] Q. Guo, C. Spitler, J.M. Sanghishetty, C.M. Boyce, Advances in vibrated gas-fluidized beds, Current Opinion in Chemical Engineering 42 (2023) 100977. https://doi.org/10.1016/j.coche.2023.100977.

- [18] Q. Guo, Y. Zhang, T.M. Kovar, K. Xi, C.M. Boyce, A Rayleigh–Bénard convection instability analog in vibrated gas-fluidized granular particles, Soft Matter (2022). https://doi.org/10.1039/D1SM01803E.
- [19] C.P. McLaren, T.M. Kovar, A. Penn, C.R. Müller, C.M. Boyce, Gravitational instabilities in binary granular materials, PNAS (2019) 201820820. https://doi.org/10.1073/pnas.1820820116.
- [20] G.H. Ristow, G. Straßburger, I. Rehberg, Phase Diagram and Scaling of Granular Materials under Horizontal Vibrations, Phys. Rev. Lett. 79 (1997) 833–836. https://doi.org/10.1103/PhysRevLett.79.833.
- [21] S.G.K. Tennakoon, L. Kondic, R.P. Behringer, Onset of flow in a horizontally vibrated granular bed: Convection by horizontal shearing, EPL 45 (1999) 470. https://doi.org/10.1209/epl/i1999-00190-3.
- [22] M. Medved, H.M. Jaeger, S.R. Nagel, Modes of response in horizontally vibrated granular matter, EPL 52 (2000) 66. https://doi.org/10.1209/epl/i2000-00405-1.
- [23] T. Zhou, H. Ogura, M. Yamamura, H. Kage, Bubble Motion Pattern and Rise Velocity in Two-dimensional Horizontal and Vertical Vibro-fluidized Beds, The Canadian Journal of Chemical Engineering 82 (2004) 236–242. https://doi.org/10.1002/cjce.5450820204.
- [24] T. Khan, M. Eslamian, Experimental analysis of one-dimensional Faraday waves on a liquid layer subjected to horizontal vibrations, Physics of Fluids 31 (2019) 082106. https://doi.org/10.1063/1.5109218.
- [25] Y. Tsuji, T. Kawaguchi, T. Tanaka, Discrete particle simulation of two-dimensional fluidized bed, Powder Technology 77 (1993) 79–87.
- [26] M.J. Andrews, P.J. O'Rourke, The multiphase particle-in-cell (MP-PIC) method for dense particulate flows, International Journal of Multiphase Flow 22 (1996) 379–402. https://doi.org/10.1016/0301-9322(95)00072-0.
- [27] J. Ding, D. Gidaspow, A bubbling fluidization model using kinetic theory of granular flow, AIChE Journal 36 (1990) 523–538. https://doi.org/10.1002/aic.690360404.
- [28] S.H.L. Kriebitzsch, M.A. van der Hoef, J.A.M. Kuipers, Fully resolved simulation of a gas-fluidized bed: A critical test of DEM models, Chemical Engineering Science 91 (2013) 1–4. https://doi.org/10.1016/j.ces.2012.12.038.
- [29] P.A. Cundall, O.D.L. Strack, A discrete numerical model for granular assemblies, Géotechnique 29 (1979) 47–65. https://doi.org/10.1680/geot.1979.29.1.47.
- [30] T.B. Anderson, R. Jackson, Fluid mechanical description of fluidized beds., Industrial & Engineering Chemistry Fundamentals 6 (1967) 527–539.
- [31] D. Gidaspow, Multiphase Flow and Fluidization: Continuum and Kinetic Theory Descriptions, Academic Press, 1994.
- [32] C.K.K. Lun, S.B. Savage, D.J. Jeffrey, N. Chepurniy, Kinetic theories for granular flow: inelastic particles in Couette flow and slightly inelastic particles in a general flowfield, Journal of Fluid Mechanics 140 (1984) 223–256. https://doi.org/10.1017/S0022112084000586.
- [33] J.M. Musser, J.E. Carney, Theoretical Review of the MFIX Fluid and Two-Fluid Models, NETL, 2020. https://doi.org/10.2172/1604993.
- [34] O. Pouliquen, C. Cassar, P. Jop, Y. Forterre, M. Nicolas, Flow of dense granular material: towards simple constitutive laws, J. Stat. Mech. 2006 (2006) P07020–P07020. https://doi.org/10.1088/1742-5468/2006/07/P07020.
- [35] F. da Cruz, S. Emam, M. Prochnow, J.-N. Roux, F. Chevoir, Rheophysics of dense granular materials: Discrete simulation of plane shear flows, Phys. Rev. E 72 (2005) 021309. https://doi.org/10.1103/PhysRevE.72.021309.
- [36] A. Srivastava, S. Sundaresan, Analysis of a frictional–kinetic model for gas–particle flow, Powder Technology 129 (2003) 72–85. https://doi.org/10.1016/S0032-5910(02)00132-8.
- [37] D.G. Schaeffer, Instability in the evolution equations describing incompressible granular flow, Journal of Differential Equations 66 (1987) 19–50. https://doi.org/10.1016/0022-0396(87)90038-6.

- [38] A. Acosta-Iborra, F. Hernández-Jiménez, M. de Vega, J.V. Briongos, A novel methodology for simulating vibrated fluidized beds using two-fluid models, Chemical Engineering Journal 198–199 (2012) 261–274. https://doi.org/10.1016/j.cej.2012.05.098.
- [39] P. Bhalode, M. Ierapetritou, A review of existing mixing indices in solid-based continuous blending operations, Powder Technology 373 (2020) 195–209. https://doi.org/10.1016/j.powtec.2020.06.043.
- [40] E. Buckingham, On Physically Similar Systems; Illustrations of the Use of Dimensional Equations, Phys. Rev. 4 (1914) 345–376. https://doi.org/10.1103/PhysRev.4.345.
- [41] S. Ergun, Fluid flow through packed beds, Chemical Engineering Progress (1952) 89–94.
- [42] C.Y. Wen, Y.H. Yu, A generalized method for predicting the minimum fluidization velocity, AIChE Journal 12 (1966) 610–612. https://doi.org/10.1002/aic.690120343.